INTERNATIONAL JOURNAL OF ADVANCED DIGITAL TECHNOLOGIES

ISSN 3125-2788 | Volume 3, Issue 1 | 2026 | pp. 1-19

https://doi.org/10.5281/zenodo.22018906 | Published online 19 August 2026

Convolutional Neural Networks Reveal Distributed Metabolic Patterns in Whole-Brain FDG-PET Images of Patients with Predominantly Negative Symptoms in Schizophrenia

From Regional Metabolic Abnormalities to Whole-Brain Signatures

Mario Enrique Molina

Universidad de Mendoza

Boulogne Sur Mer 683, Ciudad, Mendoza, Argentina, CP 5500

Correspondence: Mario Enrique Molina | mario.molina@um.edu.ar | molinario@gmail.com

EDITORIAL DISCLOSURE AND PEER-REVIEW STATUS. The sole author, Mario Enrique Molina, is the founding editor of IJADT. This editor-authored contribution was accepted and published by an explicit editorial decision of the author in his editorial capacity. It did not undergo independent external peer review by IJADT, and no claim of independent editorial adjudication is made. This dual role is disclosed so that readers may evaluate the work with full knowledge of its editorial circumstances. The author assumes full responsibility for the study, its interpretation, and the decision to publish.

Abstract

Objectives: To determine whether distributed whole-brain FDG-PET patterns distinguish patients with schizophrenia characterised by predominantly negative symptoms from healthy controls and whether classifier-associated anatomy is reproducible.

Methods: Historical, de-identified PET volumes from six patients and six controls were analysed using a compact 3D convolutional neural network (4,473 trainable parameters). Exhaustive leave-one-control/leave-one-patient-out evaluation comprised 36 folds per run and was repeated under three optimisation trajectories. Masks, scaling factors and metabolic effect-size maps were derived exclusively from each training set. Class activation maps were combined with training-derived Cohen's d maps to identify spatial convergence.

Results: Held-out accuracy ranged from 95.83% to 100%, with area under the receiver operating characteristic curve (AUC) values of 0.9923–1.0000. Multiseed subject-level consensus completely separated controls from patients. The consensus convergence cluster contained 2,169 voxels, of which 1,767 (81.5%) formed a stable three-run core. Its peak was located in the right precentral gyrus/BA6, within a predominantly right frontal, sensorimotor and temporoparietal territory.

Conclusions: Whole-brain FDG-PET contained internally consistent discriminatory information in this cohort. The reproducible anatomical territory supports a distributed network interpretation, but the small sample precludes population-level diagnostic claims and requires external validation.

Keywords: Schizophrenia; Fluorodeoxyglucose F18; Positron-Emission Tomography; Deep Learning; Brain Mapping.

Introduction

Schizophrenia is a severe and biologically complex psychiatric disorder whose clinical expression encompasses positive, negative, and cognitive dimensions. Negative symptoms comprise reductions in motivation, pleasure, social engagement, emotional expression, and speech, and are commonly assessed together with positive and general psychopathology using the Positive and Negative Syndrome Scale (PANSS) (Kay et al. 1987). Unlike positive symptoms, which are often episodic and comparatively responsive to antipsychotic treatment, negative symptoms may persist across the course of illness and remain difficult to treat. Their clinical importance extends beyond symptom burden: primary negative symptoms are independently associated with impaired social, occupational, and everyday functioning (Fervaha et al. 2014). A better understanding of their neural substrates is therefore important for both biological models and the development of more effective interventions.

Three-dimensional convolutional neural networks (3D CNNs) offer a complementary approach by learning distributed spatial features directly from whole-brain neuroimaging volumes and testing whether those features support individual-level classification (Litjens et al. 2017). When combined with spatial interpretability methods such as class activation mapping, these models can also indicate which anatomical patterns contribute to their predictions (Zhou et al. 2016). Convolutional neural networks have previously been applied to brain FDG-PET imaging, particularly in neurodegenerative disorders, including classification of Alzheimer's disease and frontotemporal dementia (Ding et al. 2019; Rogeau et al. 2024).

Neuroimaging findings suggest that negative symptoms do not arise from dysfunction of a single brain structure. Abnormalities have been reported in prefrontal, temporal, limbic, cerebellar, thalamic, and basal-ganglia systems, supporting models of schizophrenia as a disorder of distributed cortico-subcortical circuits (Weinberger et al. 1992; Goldman-Rakic and Selemon 1997; Andreasen et al. 1998). FDG-PET studies have further related predominantly negative symptomatology to altered metabolism in frontal, temporal, and cerebellar regions (Potkin et al. 2002). Collectively, these observations are consistent with disruption of networks that integrate motivation and contextual information with the selection, initiation, and monitoring of goal-directed behaviour.

Our previous FDG-PET investigation examined regional cerebral glucose metabolism in patients with schizophrenia characterised by predominantly negative symptoms (Galeno et al. 2004). Using Statistical Parametric Mapping (SPM), patients were stratified according to negative-symptom severity and compared with healthy controls. Mildly affected patients showed abnormalities involving prefrontal, cingulate, sensorimotor, occipital, and temporal regions, whereas severely affected patients showed prominent cortical and subcortical abnormalities, including increased activity in the left globus pallidus and right claustral/insular territory. These findings suggested that symptom severity was associated with altered cortico-striato-pallido-thalamic and related neural systems. The original analysis, however, was designed to identify group-level regional differences and could not determine whether whole-brain metabolic configurations contained information capable of discriminating individual participants.

Advances in convolutional neural networks (CNNs) now provide a complementary framework for addressing this question. Whereas conventional voxelwise analyses test where groups differ, CNNs can learn distributed spatial representations directly from volumetric images and evaluate whether those representations support individual classification. Three-dimensional CNNs have consequently been applied across medical imaging, although their use in small neuroimaging cohorts requires strict separation of training and test information, constrained model complexity, and cautious interpretation (Litjens et al. 2017). Architectures that combine convolutional feature extraction with global average pooling also permit class activation mapping, enabling the spatial evidence contributing to a classification decision to be examined without relying solely on prediction accuracy (Zhou et al. 2016).

The availability of the original three-dimensional FDG-PET volumes offered an unusual opportunity to revisit the same biological dataset using methods that were not practically available when it was acquired. Rather than attempting to reproduce the historical SPM analysis, the present study addressed a distinct, individual-level question. Whole-brain PET volumes from patients with schizophrenia characterised by predominantly negative symptoms and healthy controls were analysed using a deliberately compact 3D CNN. Classification was evaluated through an exhaustive paired held-out procedure in which every possible control-patient pair was excluded from model development and subsequently classified. All preprocessing quantities were derived exclusively from each training set, and

the complete experiment was repeated with independent random initialisations to assess the stability of both prediction and anatomical localisation.

The study had three objectives: first, to determine whether distributed whole-brain FDG-PET patterns could discriminate individual patients from controls; second, to assess whether classification and anatomical localisation were reproducible across independent training runs; and third, to compare the spatial evidence learned by the CNN with training-derived voxelwise metabolic effect sizes. By identifying regions in which metabolic abnormality and classifier-associated information converged, we sought to extend the original group-based findings towards a reproducible individual-level representation, while recognising that the small historical cohort permits assessment of internal consistency but not estimation of population-level diagnostic performance.

Methods

Study cohort and clinical assessment

The source study was conducted at the Instituto de Neurociencias and Fundación Escuela de Medicina Nuclear (FUESMEN), Mendoza, Argentina. A clinical pool of 47 outpatients was assessed with the Positive and Negative Syndrome Scale (PANSS) after a five-day medication washout. The historical PET cohort comprised 14 patients with schizophrenia (10 men and 4 women; age range, 18-67 years; mean age, 39 years) and six healthy controls (age range, 23-49 years; mean age, 35 years) with a similar sex distribution. Patients met Diagnostic and Statistical Manual of Mental Disorders, Fourth Edition (DSM-IV) criteria for schizophrenia. Diagnosis was established through clinical interviews conducted independently by two psychiatrists. Exclusion criteria included pregnancy, schizoaffective disorder, neurological disease, alcoholism, and drug abuse. The original human study was approved under the institutional ethical procedures in force at the participating institutions and was conducted in accordance with the ethical principles of the Declaration of Helsinki. All participants provided written informed consent for the original PET study (Galeno et al. 2004). The present investigation was a retrospective secondary analysis of previously acquired, de-identified images and involved no new participant recruitment, intervention, or image acquisition.

Patients with a PANSS positive-subscale score below 20 and a negative-subscale score of at least 25 were considered to have predominantly negative symptomatology. Negative-symptom severity was classified as moderately high (mildly affected in the historical terminology) for negative-subscale scores of 25-39 and severe for scores above 40. The historical cohort included 10 moderately affected and four severely affected patients. For the present analysis, six patients were selected to provide balanced representation of the two predefined negative-symptom severity strata: three moderately affected and three severely affected patients. These six patients and all six available healthy controls formed two balanced groups of six participants. The binary classification task distinguished the patient group from the control group. Because this is a secondary analysis of a small historical cohort, all cross-validation procedures were defined at the biological-subject level. Cohort derivation and composition are summarised in Table 1.

Table 1. Derivation and composition of the study cohort

Stage	Definition	Number
Original clinical pool	Outpatients assessed with PANSS after a five-day medication washout	47
Historical predominantly negative cohort	PANSS positive subscale <20 and PANSS negative subscale >=25	14
Moderately affected stratum	PANSS negative subscale 25-39	10
Severely affected stratum	PANSS negative subscale >40	4
Present patient sample	Selected to provide balanced representation of the severity strata: 3 moderately affected and 3 severely affected patients	6
Control sample	All available healthy controls	6
Final CNN cohort	Patient group plus control group	12

PANSS, Positive and Negative Syndrome Scale; CNN, convolutional neural network.

PET acquisition

Brain glucose metabolism was measured at FUESMEN, Mendoza, Argentina, with [18F]fluorodeoxyglucose ([18F]FDG) positron emission tomography (PET) using a QUEST scanner

(UGM Inc., Philadelphia, PA, USA) in three-dimensional acquisition mode. Each participant was positioned with the head aligned to the scanner laser system and received 5 mCi of [18F]FDG intravenously. During uptake and acquisition, participants remained awake with eyes open and ears uncovered in a quiet, dimly lit room. One-millilitre blood samples were obtained for determination of plasma FDG concentrations. The acquisition procedure was identical to that reported for the source cohort (Galeno et al. 2004).

Image preprocessing

The present analysis used the historical PET volumes available from the original study. These images had previously undergone spatial normalisation to a common stereotaxic template and smoothing with an isotropic Gaussian kernel (12-mm full width at half maximum) as part of the original SPM-based processing pipeline (Friston et al. 1995; Galeno et al. 2004).

For the current machine-learning analysis, the normalised images were represented on a 79 × 95 × 68 voxel grid. Each PET volume then underwent fold-specific preprocessing. First, individual SPM-style global intensity normalisation was applied. A preliminary whole-volume mean was calculated, and the SPM global estimate was defined as the mean activity of voxels exceeding one eighth of that preliminary mean. The complete volume was then rescaled so that this global estimate equalled 50 arbitrary units (SPM50). Subsequently, fold-specific brain masks and intensity scaling procedures were derived exclusively from the training data, as described below.
Within each held-out fold, a strict brain mask was derived exclusively from the ten training subjects by retaining voxels whose SPM50 intensity was greater than 40 in every training image, corresponding to a relative threshold of 0.80 with respect to the target global value of 50. The 99.5th percentile of voxel intensities pooled across all training images within this training-derived mask was then used as the common scaling denominator. The mask and denominator were applied unchanged to both the training and held-out images; no additional clipping of the scaled PET inputs to [0, 1] was performed. Thus, held-out subjects contributed neither to mask construction nor to scaling-factor estimation.

Compact three-dimensional convolutional neural network

A compact three-dimensional convolutional neural network (3D CNN) received one whole-brain PET volume per subject. The feature extractor comprised three 3 x 3 x 3 convolutional layers with same padding, rectified linear unit activation, and 4, 8, and 16 filters, respectively. The first two convolutional layers were followed by max-pooling. Global average pooling converted the final feature maps to a 16-element vector, which was connected to a single sigmoid output unit estimating the probability of schizophrenia. The model contained 4,473 trainable parameters.

Training used binary cross-entropy loss and the Adam optimiser with a learning rate of 0.001 (Kingma and Ba 2015). The batch size was one, and probabilities of 0.50 or greater were classified as schizophrenia. No atlas labels, clinical scores, or handcrafted regional features were supplied to the network.

Exhaustive paired held-out evaluation

Internal held-out discrimination was evaluated with an exhaustive leave-one-control/leave-one-patient-out design. For each of the 36 possible control-patient pairs, one control and one patient were held out together, leaving five controls and five patients for training. Each run therefore comprised 36 independently fitted models and generated 72 held-out predictions. Every biological subject was held out six times, once with each member of the opposite diagnostic group. These repeated predictions are procedural replicates of the same subject rather than independent observations.

Subject-level consensus scores were calculated as the mean of the six held-out probabilities obtained for each participant. Performance was summarised by accuracy, balanced accuracy, sensitivity, specificity, area under the receiver operating characteristic curve (AUC), Matthews correlation coefficient (MCC), and the confusion matrix. The subject-level consensus analysis was treated as the principal evaluation because its unit of inference was the biological subject.

Multiseed analysis

To examine stability with respect to stochastic optimisation, the complete 36-fold evaluation was repeated with three random seeds. Seed 42 was trained for 200 epochs, whereas seeds 123 and 456 were trained for 100 epochs. The same folds, preprocessing rules, architecture, optimiser, and decision threshold were used in all runs. Because training duration differed between the first and subsequent runs, agreement across runs was interpreted as combined robustness to random initialisation and the specified training schedules, rather than as an isolated seed effect.

Class activation mapping and metabolic effect sizes

For each trained model, a separate signed class activation map (CAM) was generated for each of the two held-out subjects from the final convolutional feature maps and the weights of the sigmoid classifier (Zhou et al. 2016). At voxel x, the low-resolution map was computed as CAM(x) = sum_k w_k A_k(x), where A_k(x) is the activation of feature map k and w_k is its output-layer weight. Each CAM was mapped back to the 79 x 95 x 68 PET grid by first-order interpolation, restricted to the fold-specific training mask, normalised by the 99th percentile of its absolute magnitude within that mask, and clipped to [-1, 1]. Positive values supported the schizophrenia class and negative values supported the control class. Absolute CAM magnitude was used only when quantifying spatial importance independently of direction.

A voxelwise Cohen d map was calculated separately within each fold from the ten training subjects only. Positive d values indicated greater PET signal in the schizophrenia group, whereas negative values indicated greater signal in controls. Estimating this map exclusively from the training set prevented the held-out images from contributing to the metabolic contrast.

Metabolic-CAM convergence and spatial reproducibility

Within each seed, spatial quantities were aggregated after completion of all 36 folds. The absolute training-only Cohen d maps were averaged voxelwise across contributing fold masks. The absolute CAMs from both held-out subjects in every fold were likewise averaged voxelwise, yielding a mean absolute held-out CAM from 72 subject-fold maps. Because fold-specific masks varied slightly, aggregation used voxelwise coverage counts. The convergence analysis was restricted to voxels represented in at least 32 Cohen d maps and at least 64 held-out CAMs. Within this robust analysis domain, the mean absolute Cohen d and mean absolute CAM values were independently converted to percentile ranks, and their voxelwise product defined the seed-level convergence score: C(x) = R|d|(x) x R|CAM|(x). The score was an exploratory measure of spatial coincidence between metabolic group differences and classifier-associated importance, without requiring directional agreement.

A single convergence map was therefore obtained for each seed after aggregation of the fold-level Cohen d and held-out CAM information. Candidate discriminative territory was defined as the top 1% of convergence values within the robust analysis domain. This threshold was used solely as a spatial summarisation rule and not as a statistical significance threshold. Spatially contiguous components were identified with 26-neighbour connectivity, and clusters smaller than 10 voxels were discarded. Reproducibility across seeds was evaluated using Dice and Jaccard overlap coefficients, voxelwise correlations of convergence maps, distances between peak coordinates, and anatomical overlap. A multiseed consensus convergence map was obtained by averaging the three seed-level maps; the stable three-seed core was defined as the voxelwise intersection of the top-1% convergence territories from all three runs.

Anatomical localisation

The consensus cluster and stable core were localised with the Automated Anatomical Labeling atlas implemented in SPM12 (AAL-SPM12), using nearest-neighbour interpolation to preserve discrete labels (Tzourio-Mazoyer et al. 2002). Coordinates were reported in Montreal Neurological Institute (MNI) space, as defined by the SPM12-normalised PET images. For each territory, voxel counts and percentages were calculated by atlas region. Talairach terminology was consulted only as an additional descriptive anatomical reference; no MNI-to-Talairach coordinate conversion was applied (Talairach and Tournoux 1988). Atlas information was used only after model fitting and did not contribute to training or prediction.

Results

Historical reference findings

The source FDG-PET cohort had previously been analysed with Statistical Parametric Mapping to identify regional metabolic abnormalities associated with predominantly negative schizophrenia and negative-symptom severity (Galeno et al. 2004). Those published findings are summarised schematically in Figure 1 and were not re-estimated as part of the present CNN analysis.

In the historical analysis, mildly affected patients showed increased metabolism relative to controls in the posterior cingulate, precentral, postcentral and occipital regions, together with decreased metabolism in prefrontal and fusiform territories. Severely affected patients showed increased metabolism in the left lateral globus pallidus, right insular and claustral regions, cuneus, bilateral postcentral gyri and right precentral cortex, with decreased metabolism predominantly in temporal regions. Direct comparison of the severe and mild subgroups identified additional superior frontal, superior temporal, subcallosal, superior parietal and left pallidal increases (Galeno et al. 2004).

Figure 1. Historical PET findings in the source cohort

A Mild vs Control

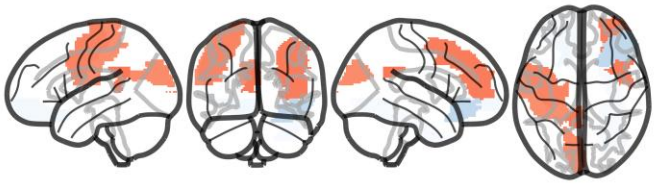

Red: higher Blue: lower

Higher metabolism

Left: Posterior cingulate gyrus (BA 31)
Right: Middle frontal gyrus (BA 6)
Left: Precentral gyrus (BA 6)
Left: Middle occipital gyrus (BA 19)
Left: Cuneus (BA 19)
Left: Postcentral gyrus (BA 3)

Lower metabolism

Right: Inferior frontal gyrus (BA 47)
Left: Orbitofrontal cortex (BA 11)
Right: Fusiform gyrus (BA 37)

B Severe vs Control

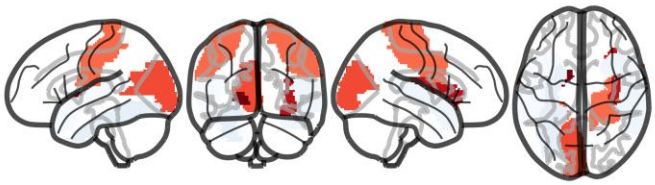

Red: higher Blue: lower

Higher metabolism

Left: Globus pallidus (lateral)
Right: Insular cortex
Left: Cuneus / calcarine fissure (BA 17)
Right: Claustrum
Bilateral: Postcentral gyrus (BA 3)
Right: Precentral gyrus (BA 6)

Lower metabolism

Left: Fusiform gyrus (BA 37)
Right: Superior temporal gyrus (BA 38)
Left: Superior temporal gyrus (BA 38)

Claustrum is listed but not projected: no separate ROI in AAL-SPM12.

C Severe vs Mild

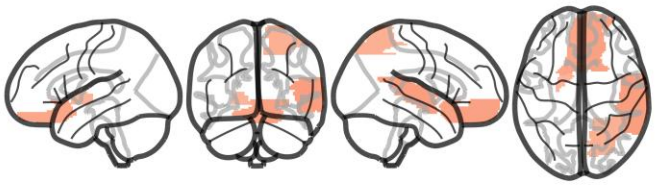

Red: higher Blue: lower

Higher metabolism

Right: Superior temporal gyrus (BA 22)
Right: Superior frontal gyrus (BA 11)
Right: Subcallosal gyrus (BA 25)
Left: Subcallosal gyrus (BA 25)
Right: Superior parietal lobe (BA 7)
Left: Globus pallidus (lateral)

Atlas-based schematic of regions reported by Galeno et al. (2004); full AAL-SPM12 regions are shown, not the original voxelwise SPM clusters.

Figure 1. Historical PET findings in the source cohort. Atlas-based schematic of the regional findings reported in the original SPM analysis (Galeno et al. 2004). The published anatomical labels were projected onto the AAL-SPM12 atlas solely for visual summarisation; the original voxelwise statistical maps were not available for reconstruction. Panels show mildly affected patients versus controls, severely affected patients versus controls, and severely versus mildly affected patients. Warm colours denote regions reported as having greater metabolism in the first named group; cool colours denote lower metabolism. The schematic does not represent the original cluster boundaries, spatial extent or test-statistic magnitude.

Exhaustive held-out classification

All 36 paired held-out folds were completed in each of the three experimental runs, yielding 72 held-out predictions per run and 216 predictions overall. The seed 42/200-epoch and seed 123/100-epoch runs each produced 69/72 correct predictions (accuracy, 0.9583; AUC, 0.9938 and 0.9923, respectively; MCC, 0.9199 for both). In both runs, all 36 patient predictions were correct and the three errors were repeated held-out evaluations of the same control subject, snp269n. The seed 456/100-epoch run classified all 72 held-out observations correctly, with accuracy, balanced accuracy, sensitivity, specificity, AUC and MCC all equal to 1.0000 (Table 2; Figure 2).

Table 2. Classification performance across independent runs

Run	Epochs	Correct	Accuracy	Balanced accuracy	Sensitivity	Specificity	AUC	MCC
Seed 42	200	69/72	0.9583	0.9583	1.0000	0.9167	0.9938	0.9199
Seed 123	100	69/72	0.9583	0.9583	1.0000	0.9167	0.9923	0.9199
Seed 456	100	72/72	1.0000	1.0000	1.0000	1.0000	1.0000	1.0000

AUC, area under the receiver operating characteristic curve; MCC, Matthews correlation coefficient. Sensitivity refers to schizophrenia and specificity to controls. The biological sample comprised 12 subjects; repeated held-out predictions are not independent biological observations.

Figure 2. Exhaustive paired held-out design and classification performance

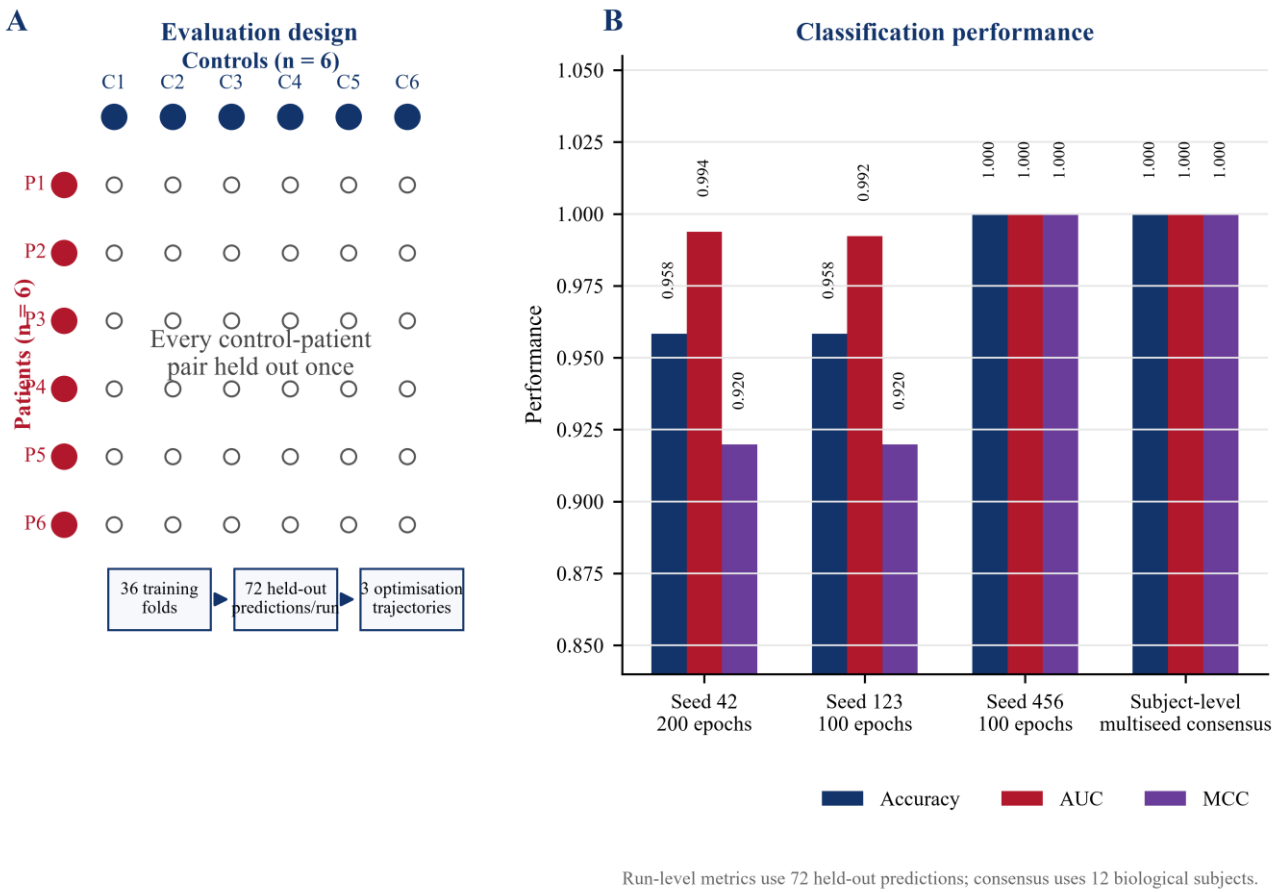

Figure 2. Exhaustive paired held-out design and classification performance. Every possible pairing of one of six controls and one of six patients was held out once, producing 36 folds and 72 held-out predictions per run. Performance is shown for seeds 42, 123 and 456 and for the 12-subject multiseed consensus. AUC, area under the receiver operating characteristic curve; MCC, Matthews correlation coefficient. The 72 predictions within a run are repeated procedural evaluations of 12 biological subjects.

Subject-level classification behaviour

Each biological subject was held out six times per run. Subject-level scores were therefore calculated within each seed as the mean of the six corresponding held-out probabilities and were then averaged across the three seeds. The six multiseed control scores ranged from 0.1508 to 0.4788, whereas the six

schizophrenia scores ranged from 0.6962 to 0.9410. The highest control score consequently remained below the lowest patient score, and the 12 subject-level consensus scores yielded accuracy = 1.0000, AUC = 1.0000 and MCC = 1.0000 (Figure 3).

Control subject snp269n remained closest to the 0.50 decision threshold. Its seed-level mean scores were 0.5069, 0.4511 and 0.4783 for seeds 42, 123 and 456, respectively, giving a multiseed consensus score of 0.4788. The subject was retained in every analysis and no post hoc exclusion or relabelling was performed.

Figure 3. Subject-level multiseed classification scores

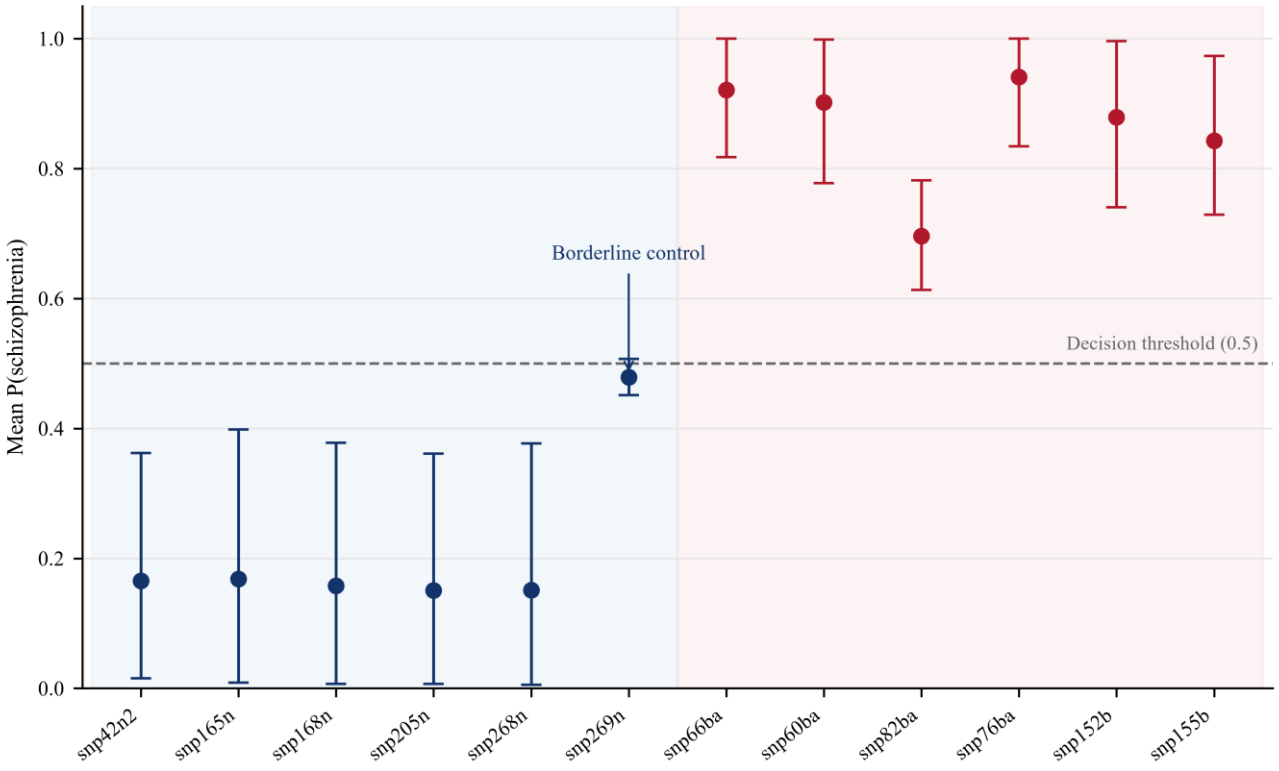

Subject	Mean	Min	Max
snp42n2	0.166	0.015	0.362
snp165n	0.168	0.009	0.398
snp168n	0.158	0.007	0.378
snp205n	0.151	0.007	0.361
snp268n	0.151	0.006	0.377
snp269n	0.479	0.451	0.507
snp66ba	0.921	0.817	1.000
snp60ba	0.902	0.778	0.999
snp82ba	0.696	0.613	0.782
snp76ba	0.941	0.834	1.000
snp152b	0.879	0.741	0.996
snp155b	0.843	0.729	0.973

Subject-level consensus: accuracy = 1.00, AUC = 1.00, MCC = 1.00.

Figure 3. Subject-level multiseed classification scores. For each seed, the subject-level score was the mean of the six probabilities obtained when that subject was held out. Points show the mean of the three seed-level subject scores; error bars span their minimum and maximum. The dashed line marks the 0.50 decision threshold. Blue denotes controls and red denotes schizophrenia. Control snp269n was closest to the threshold but was retained without post hoc exclusion.

Multiseed spatial reproducibility

Mean absolute CAM maps showed variable correspondence across runs, with pairwise voxelwise correlations ranging from 0.506 to 0.927. Signed true-class CAM correlations ranged from 0.376 to 0.910. Convergence maps were more consistent, with pairwise correlations of 0.652-0.966 and top-1% convergence Dice coefficients of 0.865-0.877 (Jaccard indices, 0.762-0.781; Table 3).

Seeds 42 and 123 had an identical principal convergence maximum at (60, -4, 42) mm. The seed 456 maximum was at (60, -6, 44) mm, 2.83 mm from the other maxima. The multiseed consensus maximum remained at (60, -4, 42) mm, where convergence was approximately 0.999, mean Cohen's d was +6.83 (schizophrenia > control) and mean absolute CAM magnitude was 0.994.

Table 3. Pairwise spatial reproducibility across independent runs

Run pair	Mean absolute CAM r	True-class CAM r	Convergence r	Top-1% Dice	Top-1% Jaccard	Peak distance (mm)
Seed 42 vs 123	0.9265	0.9098	0.9659	0.8728	0.7742	0.00
Seed 42 vs 456	0.5722	0.4946	0.6774	0.8769	0.7808	2.83
Seed 123 vs 456	0.5064	0.3764	0.6521	0.8649	0.7620	2.83

CAM, class activation map. Correlations are pairwise voxelwise spatial correlations. Dice and Jaccard coefficients quantify overlap of the seed-level top-1% convergence territories. Top 1% was a spatial summarisation rule, not a statistical significance threshold.

Stable multiseed anatomical territory

The top 1% of the multiseed consensus convergence map formed a principal cluster of 2,169 voxels. Of these, 1,767 voxels also belonged to the top-1% convergence territory in every individual seed, constituting 81.5% of the consensus cluster. A separate top-1% CAM core shared by all three runs contained 1,208 voxels.

The consensus maximum was localised to the right precentral gyrus and Brodmann area 6. The consensus cluster was predominantly right-sided, with its largest contributions in the middle frontal (28.49%), precentral (14.06%), postcentral (12.40%), inferior frontal triangular (11.16%), middle temporal (10.97%), supramarginal (8.39%) and superior temporal (7.19%) regions. The stable three-seed core had a closely corresponding anatomical composition (Table 4; Figure 4).

Table 4. Anatomical composition of the consensus convergence cluster and stable three-seed core

AAL-SPM12 region	Consensus cluster, %	Consensus voxels	Stable core, %	Stable-core voxels
Frontal_Mid_R	28.49	618	29.09	514
Precentral_R	14.06	305	14.37	254
Postcentral_R	12.40	269	12.96	229
Frontal_Inf_Tri_R	11.16	242	11.49	203
Temporal_Mid_R	10.97	238	10.70	189
SupraMarginal_R	8.39	182	8.66	153
Temporal_Sup_R	7.19	156	7.07	125
Frontal_Inf_Oper_R	4.06	88	4.30	76
Angular_R	1.52	33	0.40	7
Parietal_Inf_R	1.15	25	0.74	13

The consensus convergence cluster contained 2,169 voxels; the stable three-seed core contained 1,767 voxels. Peak consensus coordinate: (60, -4, 42) mm in MNI space, labelled Precentral_R / Brodmann area 6. Percentages are calculated within the corresponding territory; rounding may affect totals.

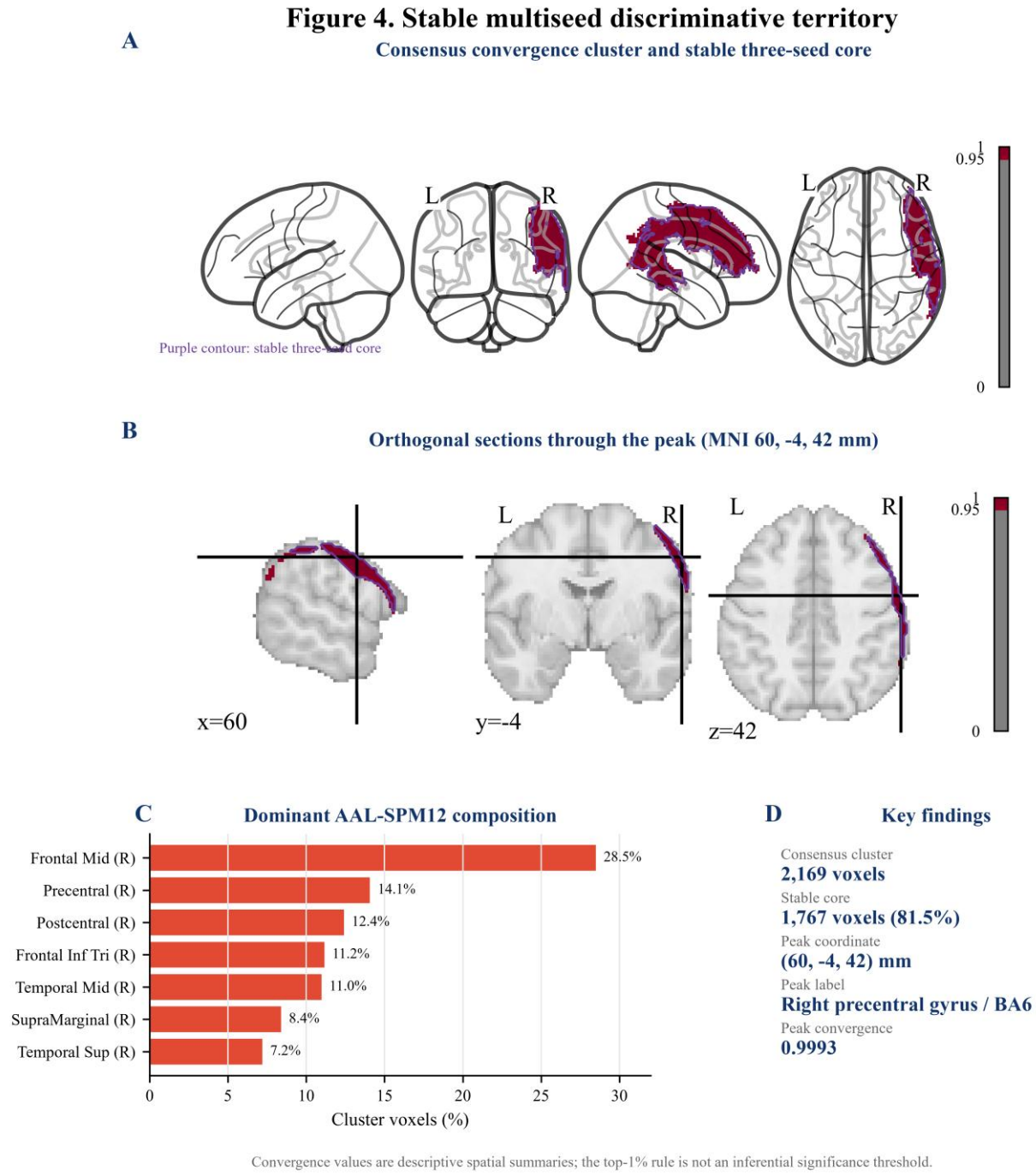

Figure 4. Stable multiseed discriminative territory. Spatial distribution of the multiseed consensus convergence territory and the core shared by all three runs, displayed in MNI space. The consensus top-1% cluster contained 2,169 voxels and the stable three-seed core 1,767 voxels. The peak at (60, -4, 42) mm was localised to the right precentral gyrus and Brodmann area 6. Colour intensity represents relative convergence rank and not statistical significance. Anatomical percentages were derived with AAL-SPM12 after model fitting.

Comparison with the historical SPM findings

Targeted comparison with the historical findings showed the strongest present convergence in the right middle frontal and right precentral territories. The right precentral region had also been identified in the original severe-versus-control comparison (Galeno et al. 2004). The left pallidum showed a relatively large present metabolic effect (mean Cohen's d approximately +1.55) but low CAM magnitude and convergence and did not enter the stable top-1% territory. The right insula showed little present case-control metabolic separation. Bilateral fusiform regions retained the historical direction of lower metabolism in schizophrenia but were not dominant contributors to the stable CNN-associated territory.

Discussion

The present study revisited a historical FDG-PET dataset using a computational framework that was not available when the images were acquired. A compact three-dimensional convolutional neural network distinguished the six patients with schizophrenia characterised by predominantly negative symptoms from six healthy controls across three exhaustive held-out experiments. More importantly, the analysis recovered a spatially coherent and reproducible territory in which training-derived metabolic group differences converged with classifier-associated information.

The near-complete held-out discrimination should not be interpreted as population-level diagnostic accuracy. It describes internal consistency within 12 biological subjects, evaluated repeatedly under a deliberately exhaustive design. The principal contribution is therefore not the numerical accuracy in isolation, but the conjunction of individual-level discrimination, strict separation of training and held-out information, and multiseed anatomical reproducibility.

From Regional Metabolic Abnormalities to Whole-Brain Signatures

The historical SPM analysis and the present CNN analysis address complementary questions. The original study asked where metabolism differed between groups and how those differences varied with negative-symptom severity (Galeno et al. 2004). The present analysis asked whether the distributed metabolic configuration of an individual brain contained information sufficient to distinguish group membership. A statistically prominent group difference need not be the most useful feature for individual classification, and a region may contribute to classification because it participates in a multiregional configuration rather than because it contains the largest isolated abnormality.

This distinction was evident in the current results. Metabolic abnormality and discriminative importance overlapped, but were not interchangeable. The convergence analysis was designed to identify locations supported by both forms of evidence: a training-only metabolic effect and strong participation in the learned representation. It should consequently be read as a spatial summary of agreement between complementary analyses, not as a causal or statistical-significance map.

A reproducible right fronto-sensorimotor and temporoparietal territory

The principal consensus cluster was predominantly right-sided and extended through middle frontal, precentral, postcentral, inferior frontal, middle and superior temporal, supramarginal, angular and inferior parietal territories. Its maximum at MNI (60, -4, 42) mm was localised to the right precentral gyrus and Brodmann area 6. Seeds 42 and 123 produced the same maximum, whereas the seed 456 maximum was displaced by only 2.83 mm. Moreover, 1,767 of the 2,169 voxels in the principal consensus cluster belonged to the top-1% territory in every run.

Raw CAM correspondence varied more across optimisation trajectories than did metabolic-CAM convergence. This difference suggests that independently trained models can implement partially different internal solutions while still recovering a common biological territory when classifier relevance is constrained by an independent metabolic contrast. The stable core is therefore best interpreted as a reproducible candidate system within this dataset, rather than as a uniquely determined disease map.

Table 5 summarises the anatomical composition of this territory, functional roles reported in the literature and the corresponding hypothesis-generating interpretation. The regions are ordered by their contribution to the stable three-seed core. The functional column does not imply that those functions were measured in the present experiment, and the clinical column distinguishes plausible relevance from demonstrated symptom-level association.

Table 5. Functional interpretation of the stable multiseed discriminative territory

Neuroanatomical region	Relative extent	Functions reported in the literature	Hypothesis-generating relevance to the present phenotype
Right middle frontal gyrus (Frontal_Mid_R)	Stable core: 29.09% (514 voxels) Consensus: 28.49% (618 voxels) Rank 1	Goal maintenance, executive monitoring, switching among alternatives and coordination of action plans. Caudal portions interface with premotor organisation (Rowe et al. 2010).	Dominant contribution supports frontal network involvement in reduced initiation and maintenance of goal-directed behaviour. Prior work links middle frontal dysfunction and prefrontal abnormalities with primary negative symptoms (Lahti et al. 2001; Wible et al. 2001).

Neuroanatomical region	Relative extent	Functions reported in the literature	Hypothesis-generating relevance to the present phenotype
Right precentral gyrus (Precentral_R; peak in BA6)	Stable core: 14.37% (254) Consensus: 14.06% (305) Rank 2 Peak MNI: (60, -4, 42) mm	Motor preparation, prospective response selection, sequencing and transformation of intention into voluntary action (Rowe et al. 2010).	Reproducible peak is compatible with impaired spontaneity, psychomotor initiation and goal-directed action. The historical PET analysis also identified precentral abnormalities, providing partial anatomical continuity.
Right postcentral gyrus (Postcentral_R)	Stable core: 12.96% (229) Consensus: 12.40% (269) Rank 3	Somatosensory processing, body representation, movement feedback and sensorimotor integration.	Extends the pattern beyond executive control to body-action integration. It may contribute to reduced motor expressivity or inefficient updating of actions, but does not demonstrate a primary somatosensory deficit.
Right inferior frontal gyrus, pars triangularis (Frontal_Inf_Tri_R)	Stable core: 11.49% (203) Consensus: 11.16% (242) Rank 4	Contextual and semantic selection, cognitive control and cooperation with temporal-parietal systems during language comprehension (Cooper et al. 2011; Smirnov et al. 2014).	Could connect the signature with alogia, reduced contextual selection and diminished communicative flexibility. The right-sided contribution may also involve nonverbal and social aspects of communication.
Right middle temporal gyrus (Temporal_Mid_R)	Stable core: 10.70% (189) Consensus: 10.97% (238) Rank 5	Semantic, audiovisual and contextual integration; interpretation of actions, narratives and socially meaningful signals.	May contribute to impoverished contextual or semantic processing and reduced responsiveness to interpersonal information. This is a network-level hypothesis, not evidence of an isolated temporal mechanism.
Right supramarginal gyrus (SupraMarginal_R)	Stable core: 8.66% (153) Consensus: 8.39% (182) Rank 6	Multisensory and sensorimotor integration, attention, imitation, body representation and contextual coupling with inferior frontal regions (Smirnov et al. 2014).	Could influence communication, perception-action coupling and social responsiveness. Its continuity with frontal, sensorimotor and temporal regions favours interpretation as a network node.
Right superior temporal gyrus (Temporal_Sup_R)	Stable core: 7.07% (125) Consensus: 7.19% (156) Rank 7	Complex auditory processing, voice and prosody, biological motion and communicative or social signals.	Could contribute to altered affective prosody, social interpretation and reciprocity. Historical temporal abnormalities provide partial continuity, although classifier relevance does not specify metabolic direction.
Right inferior frontal gyrus, pars opercularis (Frontal_Inf_Oper_R)	Stable core: 4.30% (76) Consensus: 4.06% (88) Rank 8	Response control, action observation and imitation, phonological processing and selective inhibition with supplementary motor and striatal systems (Smittenaar et al. 2013).	May relate to reduced facial or vocal expression and response initiation. Altered relationships between empathy and right opercular activity have been reported in schizophrenia (Horan et al. 2014).
Right angular gyrus (Angular_R)	Stable core: 0.40% (7) Consensus: 1.52% (33) Rank 9 by consensus	Multimodal integration, semantic memory, attentional reorientation, perspective taking and contextual interpretation.	Small and less stable contribution may support social-context and perspective processes. It should be treated as a secondary edge of the network, not a principal focus.
Right inferior parietal lobule (Parietal_Inf_R)	Stable core: 0.74% (13) Consensus: 1.15% (25) Rank 10	Integration of attention, sensory evidence and action plans; updating of representations across frontoparietal systems.	Completes the frontoparietal component of the signature. Inferior parietal underactivation has been reported in deficit schizophrenia (Lahti et al. 2001), but the present extent is small and should be interpreted as complementary.

Note. Regions are ordered by their proportion in the stable three-seed core (1,767 voxels); consensus-cluster values refer to the principal 2,169-voxel convergence cluster. Percentages describe anatomical composition, not effect magnitude or statistical significance. 'Relevance' is interpretive and does not imply lesion, uniform metabolic direction, symptom specificity or causality. CAM, class activation map; MNI, Montreal Neurological Institute.

A proposed processing account of predominantly negative symptomatology

The regional distribution supports a processing account that links cognitive control to action and expression. The dominant right middle frontal component may contribute to maintaining goals, monitoring prior actions and switching between alternatives, while inferior frontal territories participate in response control and contextual selection. Middle frontal and inferior parietal underactivation has previously been reported in deficit schizophrenia, and prefrontal measures have been related to negative-symptom severity (Lahti et al. 2001; Wible et al. 2001). These associations make the frontal predominance biologically plausible, but they do not establish that the present cluster encodes avolition or any other single symptom.

The reproducible BA6/precentral maximum and the substantial postcentral contribution extend the interpretation from abstract control towards the transformation of intention into action. Premotor systems participate in prospective response selection and preparation, whereas lateral prefrontal systems are more strongly implicated in monitoring and switching among alternatives (Rowe et al. 2010). Inferior frontal, supplementary motor and striatal structures also participate in proactive response control (Smittenaar et al. 2013). The adjoining postcentral territory may provide somatosensory and body-state information

required to update an unfolding action. In a predominantly negative phenotype, disruption across this frontal-sensorimotor interface could plausibly contribute to reduced spontaneity, psychomotor slowing and difficulty initiating or sustaining goal-directed behaviour.

The temporal and inferior parietal extension adds a communicative and contextual dimension. Inferior frontal, temporal and parietal regions cooperate during interpretation-dependent language and context-dependent speech comprehension (Cooper et al. 2011; Smirnov et al. 2014). The right inferior frontal region has also shown altered relationships with empathy during observation of emotional expressions in schizophrenia (Horan et al. 2014). Within the present anatomical pattern, these territories could contribute to impoverished speech, reduced prosodic or emotional expression, diminished social engagement and difficulty translating interpersonal context into an adaptive response.

Taken together, the findings motivate a network hypothesis: negative symptoms may partly reflect inefficient coupling between representation of goals and context, selection and preparation of action, sensorimotor feedback, and the expression of socially meaningful behaviour. Aberrant striato-cortical connectivity associated with negative-symptom severity provides independent support for considering motivation and action selection as network-level processes (Reckless et al. 2015). This account remains inferential. The present binary classification did not model individual symptom domains, and PANSS negative scores combine clinically distinct features such as avolition, anhedonia, asociality, blunted affect and alogia.

Continuity and divergence from the historical PET findings

The right precentral and bilateral postcentral findings provide the clearest anatomical continuity with the historical study. Their recurrence is notable because the CNN received no atlas labels, predefined regions or historical statistical results during training. The correspondence was identified only after model fitting and therefore represents convergence between analytically independent approaches applied to the same biological source material.

The new analysis did not simply reproduce the historical map. The left globus pallidus retained a substantial case-control metabolic effect but showed comparatively low CAM magnitude and convergence, and it did not enter the stable top-ranking territory. The right insula likewise showed little separation in the present case-control contrast despite its prominence in the historical severity-defined comparison. These differences are not contradictions: a structure may be metabolically abnormal, or related to symptom severity, without being among the features that most efficiently distinguish an individual patient when the model can use the complete three-dimensional pattern.

The combined evidence is therefore more compatible with interacting circuits than with a single anatomical focus. Prefrontal, premotor, somatosensory, temporal and parietal regions may participate in a distributed cortical system, while pallidal, striatal, insular and thalamic structures modulate related loops. This interpretation is consistent with circuit-based accounts of schizophrenia (Goldman-Rakic and Selemon 1997; Andreasen et al. 1998), but the present data cannot determine the direction of influence among nodes.

An integrative interpretation is that the historical and current analyses capture complementary components of the same distributed system. The 2004 SPM analysis identified regions whose mean metabolism differentiated groups or varied with negative-symptom severity, whereas the present CNN analysis identified the multiregional configuration most informative for individual discrimination. Their overlap in precentral and postcentral cortex, together with the lower present discriminative prominence of pallidal and insular findings, raises the testable hypothesis that cortical frontal-sensorimotor-temporoparietal organisation may contribute to a relatively stable individual signature, while subcortical and insular components more strongly modulate symptom severity or clinical state. This distinction should be tested directly rather than inferred from the present small sample.

Hemispheric organisation and individual heterogeneity

The stable territory was overwhelmingly right-sided. This asymmetry may be relevant to nonverbal expression, prosody, bodily integration, response control and social-context processing, all of which could influence the clinical appearance of negative symptoms. Nevertheless, laterality should be interpreted cautiously because it may depend on phenotype, task state, analytical contrast, spatial normalisation and sampling. Classifier-derived asymmetry also has a different meaning from hemispheric

differences in absolute metabolism. Replication with independent data and explicit left-right tests is required.

Control subject snp269n further illustrates the value of subject-level analysis. This participant repeatedly produced scores closer to the decision boundary than the remaining controls, yet remained on the control side in the multiseed consensus. The subject was retained in every analysis and no post hoc exclusion or relabelling was performed. Without additional clinical information, this behaviour cannot be interpreted as occult pathology. It instead demonstrates that exhaustive held-out evaluation can reveal individual heterogeneity that would be obscured by a single train-test partition.

Methodological considerations, limitations and future experiments

Several design features strengthen the internal interpretation. The network was restricted to 4,473 trainable parameters; every possible control-patient pair was held out once per run; the brain mask, scaling denominator and metabolic effect-size map were derived exclusively from each training set; and the complete 36-fold procedure was repeated under three optimisation trajectories. Subject-level consensus, rather than 72 procedurally repeated predictions, was treated as the principal unit of evaluation. The analysis also separated prediction performance from spatial reproducibility.

The small sample remains the dominant limitation. Six patients and six controls cannot estimate population-level generalisation, accommodate the biological heterogeneity of schizophrenia or support reliable symptom-domain modelling. External validation in a substantially larger and independently acquired FDG-PET cohort is required before considering diagnostic or prognostic use. The historical scanner, reconstruction, medication washout, diagnostic framework and preprocessing choices may also limit transfer to contemporary datasets.

Training duration differed across runs: seed 42 used 200 epochs, whereas seeds 123 and 456 used 100. Agreement therefore reflects robustness across the combined optimisation conditions rather than an isolated random-seed effect. Future experiments should hold the training schedule constant, predefine all hyperparameters within nested training procedures, and test whether the spatial core remains stable across architectures and attribution methods.

CAM and metabolic-CAM convergence are associative interpretability tools. They identify where classifier-associated information and group differences coincide, but they do not prove necessity, sufficiency or causal pathophysiology. The top-1% threshold was a spatial summarisation rule rather than an inferential threshold. Replication should include perturbation or occlusion analyses, uncertainty estimates and comparison with non-neural confounds.

The most informative next step is dimensional rather than purely diagnostic. Larger datasets could test whether the proposed frontal-sensorimotor-temporoparietal system predicts avolition, blunted expression, alogia, anhedonia and asociality separately; whether severity-related pallidal or insular effects re-emerge when mild and severe groups are modelled directly; and whether connectivity among cortical and subcortical nodes explains more variance than regional intensity alone. Longitudinal or treatment-response designs could further distinguish stable vulnerability from state-dependent expression.

A second look at the same brains

The biological data in this study are not new, but the question asked of them is. The historical analysis identified regional metabolic abnormalities; the present analysis indicates that the distributed whole-brain configuration also contains internally consistent information capable of distinguishing individual participants. The two approaches overlap anatomically without being equivalent.

In this small historical cohort, the most reproducible individual-level signature was a right-dominant frontal, sensorimotor and temporoparietal territory centred on precentral BA6. The findings support a circuit-level account in which impaired coordination of goals, contextual interpretation, action preparation, bodily feedback and expressive behaviour may contribute to predominantly negative symptomatology. This model is hypothesis-generating and requires direct symptom-level testing and external validation.

Conclusions

Reanalysis of a historical FDG-PET cohort with a compact three-dimensional convolutional neural network showed that distributed whole-brain metabolic patterns contained internally consistent

information capable of distinguishing the six patients with schizophrenia characterised by predominantly negative symptoms from six healthy controls. Exhaustive paired held-out evaluation and repetition across three optimisation trajectories produced near-complete discrimination, while the held-out participants remained excluded from mask construction, intensity scaling and metabolic effect-size estimation.

The most reproducible classifier-associated territory was predominantly right-sided, centred on the right precentral gyrus and Brodmann area 6, and extended through frontal, sensorimotor and temporoparietal regions. Its partial correspondence with the historical PET findings, together with divergence in pallidal and insular contributions, indicates that group-level metabolic abnormalities and features useful for individual discrimination are related but not interchangeable. The pattern favours a distributed circuit-level account linking goal and context representation, action selection and preparation, somatosensory feedback, and socially meaningful expression.

These results do not establish a diagnostic biomarker, causal pathophysiology or symptom-domain specificity. The sample of 12 historical participants precludes population-level claims and requires validation in substantially larger, independently acquired cohorts. Future studies should use standardised training schedules, dimensional modelling of negative-symptom domains and complementary attribution and perturbation analyses. Within these limits, the study illustrates how modern computational methods can provide a second, individually oriented reading of archived neuroimaging data.

Acknowledgements

The author gratefully acknowledges Fundacion Escuela de Medicina Nuclear (FUESMEN), Mendoza, Argentina, for the historical acquisition and institutional stewardship of the PET images used in this secondary analysis.

The author used ChatGPT 5.6 Sol (OpenAI) to assist with language refinement, editorial organisation and reference checking during manuscript preparation. The tool was not used to generate or analyse study data, execute the computational pipeline, or create or manipulate the scientific figures. The author reviewed and confirmed the originality and accuracy of the manuscript, verified the references, checked the tool's terms of use and suitability for publication, and takes full responsibility for the integrity of the content.

Statement of Interest

The author is the founding editor of IJADT. This editorial relationship constitutes a conflict of interest for the handling of this article and is disclosed in the editorial statement above. No independent IJADT editor adjudicated acceptance. No financial conflict of interest is declared.

Funding

This research received no specific grant from any funding agency in the public, commercial or not-for-profit sectors.

Data availability statement

The de-identified data and supporting materials are not publicly available because they derive from a historical clinical cohort and remain subject to institutional authorisation. Reasonable requests may be considered with permission from FUESMEN and any other applicable institutional authority.

References

Andreasen NC, Paradiso S, O'Leary DS. 1998. Cognitive dysmetria as an integrative theory of schizophrenia: a dysfunction in cortical-subcortical-cerebellar circuitry. Schizophr Bull. 24(2):203-218. doi:10.1093/oxfordjournals.schbul.a033321.

Cooper EA, Hasson U, Small SL. 2011. Interpretation-mediated changes in neural activity during language comprehension. NeuroImage. 55(3):1314-1323. doi:10.1016/j.neuroimage.2011.01.003.

Ding Y, Sohn JH, Kawczynski MG, Trivedi H, Harnish R, Jenkins NW, et al. 2019. A deep learning model to predict a diagnosis of Alzheimer disease by using 18F-FDG PET of the brain. Radiology. 290(2):456-464. doi:10.1148/radiol.2018180958.

Fervaha G, Foussias G, Agid O, Remington G. 2014. Impact of primary negative symptoms on functional outcomes in schizophrenia. Eur Psychiatry. 29(7):449-455. doi:10.1016/j.eurpsy.2014.01.007.

Friston KJ, Holmes AP, Worsley KJ, Poline JB, Frith CD, Frackowiak RSJ. 1995. Statistical parametric maps in functional imaging: a general linear approach. Hum Brain Mapp. 2(4):189-210. doi:10.1002/hbm.460020402.

Galeno R, Molina M, Guirao M, Isoardi R. 2004. Severity of negative symptoms in schizophrenia correlated to hyperactivity of the left globus pallidus and the right claustrum: a PET study. World J Biol Psychiatry. 5(1):20-25. doi:10.1080/15622970410029903.

Goldman-Rakic PS, Selemon LD. 1997. Functional and anatomical aspects of prefrontal pathology in schizophrenia. Schizophr Bull. 23(3):437-458. doi:10.1093/schbul/23.3.437.

Horan WP, Iacoboni M, Cross KA, Korb A, Lee J, Nori P, et al. 2014. Self-reported empathy and neural activity during action imitation and observation in schizophrenia. NeuroImage Clin. 5:100-108. doi:10.1016/j.nicl.2014.06.006.

Kay SR, Fiszbein A, Opler LA. 1987. The Positive and Negative Syndrome Scale (PANSS) for schizophrenia. Schizophr Bull. 13(2):261-276. doi:10.1093/schbul/13.2.261.

Kingma DP, Ba J. 2015. Adam: a method for stochastic optimization. In: Proceedings of the 3rd International Conference on Learning Representations (ICLR 2015). arXiv:1412.6980. doi:10.48550/arXiv.1412.6980.

Lahti AC, Holcomb HH, Medoff DR, Weiler MA, Tamminga CA, Carpenter WT Jr. 2001. Abnormal patterns of regional cerebral blood flow in schizophrenia with primary negative symptoms during an effortful auditory recognition task. Am J Psychiatry. 158(11):1797-1808. doi:10.1176/appi.ajp.158.11.1797.

Litjens G, Kooi T, Bejnordi BE, Setio AAA, Ciompi F, Ghafoorian M, et al. 2017. A survey on deep learning in medical image analysis. Med Image Anal. 42:60-88. doi:10.1016/j.media.2017.07.005.

Potkin SG, Alva G, Fleming K, Anand R, Keator D, Carreon D, et al. 2002. A PET study of the pathophysiology of negative symptoms in schizophrenia. Am J Psychiatry. 159(2):227-237. doi:10.1176/appi.ajp.159.2.227.

Reckless GE, Andreassen OA, Server A, Ostefjells T, Jensen J. 2015. Negative symptoms in schizophrenia are associated with aberrant striato-cortical connectivity in a rewarded perceptual decision-making task. NeuroImage Clin. 8:290-297. doi:10.1016/j.nicl.2015.04.025.

Rogeau A, Hives F, Bordier C, Lahousse H, Roca V, Lebouvier T, et al. 2024. A 3D convolutional neural network to classify subjects as Alzheimer's disease, frontotemporal dementia or healthy controls using brain 18F-FDG PET. NeuroImage. 288:120530. doi:10.1016/j.neuroimage.2024.120530.

Rowe JB, Hughes L, Nimmo-Smith I. 2010. Action selection: a race model for selected and non-selected actions distinguishes the contribution of premotor and prefrontal areas. NeuroImage. 51(2):888-896. doi:10.1016/j.neuroimage.2010.02.045.

Smirnov D, Glerean E, Lahnakoski JM, Salmi J, Jaaskelainen IP, Sams M, et al. 2014. Fronto-parietal network supports context-dependent speech comprehension. Neuropsychologia. 63:293-303. doi:10.1016/j.neuropsychologia.2014.09.007.

Smittenaar P, Guitart-Masip M, Lutti A, Dolan RJ. 2013. Preparing for selective inhibition within frontostriatal loops. J Neurosci. 33(46):18087-18097. doi:10.1523/JNEUROSCI.2167-13.2013.

Talairach J, Tournoux P. 1988. Co-planar stereotaxic atlas of the human brain. Stuttgart (Germany): Thieme.

Tzourio-Mazoyer N, Landeau B, Papathanassiou D, Crivello F, Etard O, Delcroix N, et al. 2002. Automated anatomical labeling of activations in SPM using a macroscopic anatomical parcellation of the MNI MRI single-subject brain. NeuroImage. 15(1):273-289. doi:10.1006/nimg.2001.0978.

Weinberger DR, Berman KF, Suddath R, Torrey EF. 1992. Evidence of dysfunction of a prefrontal-limbic network in schizophrenia: a magnetic resonance imaging and regional cerebral blood flow study of discordant monozygotic twins. Am J Psychiatry. 149(7):890-897. doi:10.1176/ajp.149.7.890.

Wible CG, Anderson J, Shenton ME, Kricun A, Hirayasu Y, Tanaka S, et al. 2001. Prefrontal cortex, negative symptoms, and schizophrenia: an MRI study. Psychiatry Res. 108(2):65-78. doi:10.1016/S0925-4927(01)00109-3.

Zhou B, Khosla A, Lapedriza A, Oliva A, Torralba A. 2016. Learning deep features for discriminative localization. In: Proceedings of the IEEE Conference on Computer Vision and Pattern Recognition; pp. 2921-2929. doi:10.1109/CVPR.2016.319.